

Core–Shell Compositional Fine Structures of Dealloyed $\text{Pt}_x\text{Ni}_{1-x}$ Nanoparticles and Their Impact on Oxygen Reduction Catalysis

Lin Gan,[†] Marc Heggen,[‡] Stefan Rudi,[†] and Peter Strasser*,^{†,§}

[†]The Electrochemical Catalysis, Energy and Materials Science Laboratory, Department of Chemistry, Technical University Berlin, 10623 Berlin, Germany

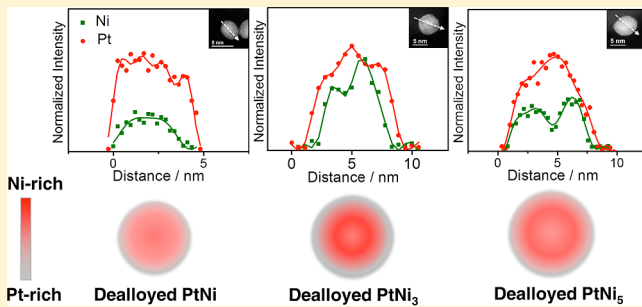
[‡]Ernst Ruska Center for Microscopy and Spectroscopy with Electrons, Forschungszentrum Juelich GmbH, 52425 Juelich, Germany

[§]Ertl Center for Electrochemistry and Catalysis, Gwanju Institute of Science and Technology (GIST), Gwanju 500 712, South Korea

Supporting Information

ABSTRACT: Using aberration-corrected scanning transmission electron microscopy and electron energy loss spectroscopy line profiles with Ångstrom resolution, we uncover novel core–shell fine structures in a series of catalytically active dealloyed $\text{Pt}_x\text{Ni}_{1-x}$ core–shell nanoparticles, showing the formation of unusual near-surface Ni-enriched inner shells. The radial location and the composition of the Ni-enriched inner shells were sensitively dependent on the initial alloy compositions. We further discuss how these self-organized Ni-enriched inner shells play a key role in maintaining surface lattice strain and thus control the surface catalytic activity for oxygen reduction.

KEYWORDS: Pt-bimetallic catalyst, core shell nanoparticles, oxygen reduction reaction, aberration-corrected scanning transmission electron microscopy, electron energy loss spectroscopy



The slow rate of the cathode oxygen reduction reaction (ORR) remains one of the main challenges for the development of polymer electrolyte membrane fuel cells (PEMFCs).^{1,2} Commercial ORR catalysts generally consist of dispersed Pt nanoparticles on high surface area carbons, which suffer from both high cost and storage limits. To become viable using Pt-based catalysts in PEMFCs, it is considered that at least a 4-fold increase of the mass activity is needed.^{2,3} Recent studies suggest that the ORR catalysis on the Pt surface is mainly hindered by overstrongly adsorbed oxygenated intermediate species, especially on low-coordinated surface sites such as steps and kinks.^{4,5} Tuning the d-band structure of Pt surfaces is expected to be an effective way to obtain weakened adsorption of oxygenated species and thus enhanced catalytic activities.^{6,7} This can be achieved by adopting transition metal atoms in the underlying atomic layers through short-range electronic interaction with Pt or through long-range geometric compressive strain effects on the Pt surface. Based on these guidelines, considerable progress has been made in the structural design of Pt-based catalysts for high catalytic activities, such as a Pt monolayer deposited on a second metal,^{8–12} and a “Pt skin” surface formed by annealing-induced segregation in Pt-transition metal alloys.^{13–15}

Dealloying, a process where less-noble metal is selectively dissolved from a bimetallic surface, has been widely studied in bulk alloys to produce nanoporous materials for catalytic applications.^{16–18} Our previous works show that, by dealloying of nanoscale transition-metal-rich Pt bimetallic or trimetallic

alloys, core–shell nanoparticles with a Pt shell and Pt alloy core were formed and showed high ORR activities.^{19,20} The compressive strain formed in the Pt shell surrounding a Pt alloy core with a smaller lattice parameter was found to play a dominant role in their high activities.²¹ A unique feature of the dealloyed core–shell catalysts is the experimental control of the lattice strain by controlling the Pt shell thickness and the alloy core composition that determines the upper limit of strain in the Pt shell, which therefore enables lattice-strain-controlled ORR activities. From this perspective, the alloy composition is considered to be one of the most important factors that determine the catalytic activities and continues to be an important subject in the research of Pt alloy electrocatalysts.^{21–32}

To further understand how alloy compositions affect the catalytic activities of dealloyed nanoparticles, detailed knowledge of the core shell fine structures at atomic scale is crucial. Recently, Wang et al. reported that the Pt-shell thickness would increase at a higher initial composition of transition metals (from 2 to ~5 atomic layers).²⁷ The difference in the Pt-shell thickness was considered to be an important factor governing the dependence of catalytic activity on the initial alloy composition. A further study on extended PtNi alloy film

Received: August 11, 2012

Revised: September 10, 2012

Published: September 14, 2012



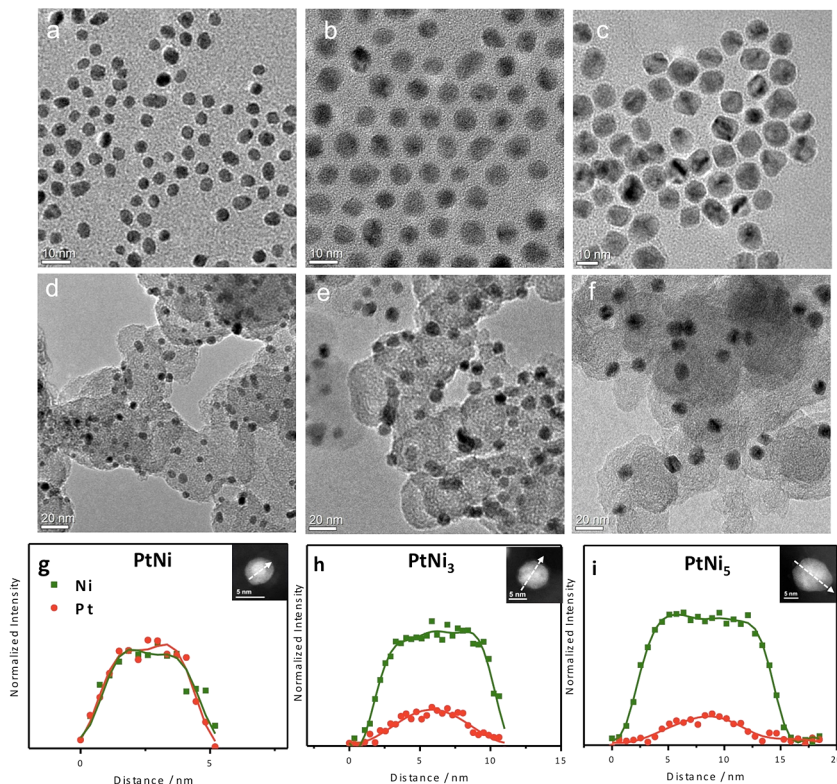


Figure 1. TEM images of (a–c) as-prepared unsupported PtNi, PtNi₃, and PtNi₅ nanoparticles and (d–f) annealed carbon supported PtNi, PtNi₃, and PtNi₅ nanoparticles, respectively. (g–i) EELS line profiles of Pt and Ni in annealed carbon supported PtNi, PtNi₃, and PtNi₅ nanoparticles. The white arrows in the corresponding nanoparticles indicate the directions of the EELS line profiles.

showed that the deposition of three atomic Pt overlayers on the alloy substrate yielded the highest ORR activity.³³ Besides the Pt shell thickness, the compositional distribution of the less noble metal below the Pt shell is another key factor in determining the catalytic activities since it controls the extent of lattice strain on the Pt surface. However, an atomic scale understanding of the compositional distribution across the alloy cores and how they would affect the catalytic activities has still remained largely unaddressed in the literature.

In this study, we uncovered core–shell fine structures formed by dealloying of a series of Pt_xNi_{1-x} nanoparticles with different Ni-rich compositions (PtNi, PtNi₃ and PtNi₅), with particular emphasis on the near-surface structure up to a depth of ~10 atomic layers. By using high-resolution aberration-corrected scanning transmission electron microscopy (STEM) and electron energy loss spectroscopy (EELS), we found that the three dealloyed Pt_xNi_{1-x} nanoparticles showed distinctly different core–shell fine structures, not only in terms of Pt shell thickness but also the compositional distribution of Ni across the alloy cores. In particular, we found strong tendency of Ni enrichment toward the near surface region at higher initial Ni compositions. The observed distinct core–shell fine structures provide new Ångstrom scale insight about how the initial composition of bimetallic nanoparticles controls their intraparticle structure in the dealloyed state and thus determines their electrocatalytic activity.

The Pt_xNi_{1-x} nanoparticles were synthesized by a modified low-temperature organic solution approach,^{27,34,35} where Pt-(acac)₂ and Ni(acac)₂ acted as the precursors, oleylamine and oleic acid as the surfactants, and 1,2-tetradecadiol as the reducing agent. Using this approach, monodisperse PtNi, PtNi₃, and PtNi₅ nanoparticles were successfully synthesized. Figure

1a–c shows typical TEM images of the PtNi, PtNi₃, and PtNi₅ nanoparticles, of which the size distributions were determined to be 5.1 ± 0.6, 8.3 ± 0.8, and 12.1 ± 1.1 nm, respectively (Figure S1a of the Supporting Information). The compositions of the nanoparticles were confirmed to be the same as the nominal ratios of the precursors using energy dispersive X-ray (EDX) and inductively coupled plasma-atomic emission spectroscopy (Table S1 and Figure S1b). The increase of the particle size as the increase of the Ni content is consistent with previous studies.^{34,35} The synthesized Pt_xNi_{1-x} nanoparticles were then supported on high surface area carbon support and heated to 180 °C in air to remove the surfactants.²⁷ To achieve a homogeneous distribution of alloy elements throughout the nanoparticles, these catalysts were further annealed at 400 °C in H₂/Ar for 4 h. TEM images show that a uniform dispersion of the Pt_xNi_{1-x} nanoparticles on the carbon supports without particle growth was achieved (Figure 1d–e). Using EELS line profile analysis, we confirmed a homogeneous distribution of Pt and Ni in individual annealed Pt_xNi_{1-x} nanoparticles (Figure 1g–i), which shows the same molar ratios of Pt to Ni as their bulk compositions (EDX).

X-ray diffraction (XRD) patterns show that all of the annealed Pt_xNi_{1-x} catalysts exhibit a single phase face-centered cubic structure (Figure 2), without the formation of ordered phase. The main peaks labeled (111) shift toward higher angle as the increase of Ni composition, which is well-known as the decrease of lattice constant by alloying of Pt with Ni. The relationship between the lattice constants derived from the XRD and the compositions of the annealed Pt_xNi_{1-x} nanoparticles (Figure S2 of the Supporting Information) shows a positive deviation from the ideal Vegard's law, consistent with previous work on bulk Pt–Ni alloys.³⁶

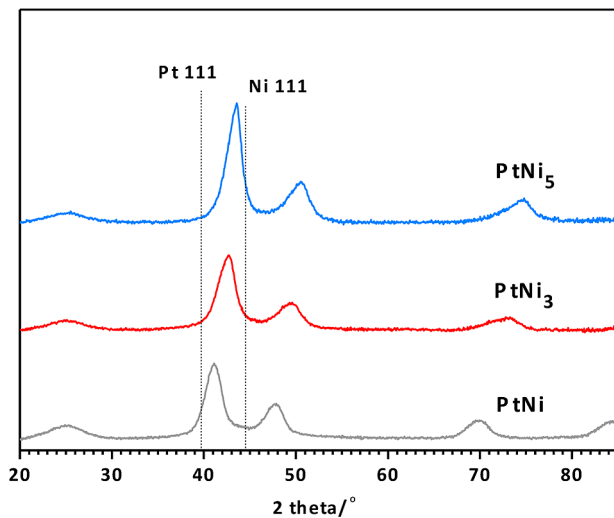


Figure 2. XRD patterns of annealed carbon supported $\text{Pt}_x\text{Ni}_{1-x}$ catalysts. The broad peaks at around 25° are from the carbon support.

The annealed carbon supported $\text{Pt}_x\text{Ni}_{1-x}$ catalysts were further electrochemically dealloyed by potential cycling between 0.06 and 1.0 V for 200 cycles at 0.5 V/s in N_2 -saturated 0.1 M HClO_4 . The dealloyed $\text{Pt}_x\text{Ni}_{1-x}$ catalysts are hereafter referred to as D-PtNi, D-PtNi₃, and D-PtNi₅, respectively. For comparison, Figure 3a and b shows the cyclic voltammograms (CVs) before and after electrochemical

dealloying, respectively. In the very initial CV (Figure 3a), PtNi catalyst shows typical Pt surface features, such as underpotential hydrogen adsorption/desorption (H_{upd}) peak between 0.06 and 0.4 V and irreversible oxidation-reduction peaks between 0.6 and 1.0 V associated with surface oxygenated species. In comparison, PtNi₃ shows a weaker H_{upd} peak, consistent with its reduced Pt:Ni ratio at the surface (Figure 1h). Meanwhile, there is a much higher oxidative peak starting from 0.4 V, which can be associated with dissolution of Ni atoms from the surface of particles. For the PtNi₅ catalyst, an even weaker H_{upd} peak was found, and the CV exhibits a typical feature of capacitance. After 200 cycles of electrochemical dealloying during which Ni dissolved completely from the surface and to a large portion from subsurface layers, all of the D-Pt_xNi_{1-x} catalysts formed a virtually pure Pt top layer and a Pt-rich near surface region and therefore showed significantly increased electrochemical surface area (ECSA) evidenced by the larger H_{upd} area (Figure 3b), which were 29 ± 2 , 35 ± 3 , and $33 \pm 3 \text{ m}^2/\text{g}_{(\text{Pt})}$ for the D-PtNi, D-PtNi₃, and D-PtNi₅, respectively. We are aware that there was an underestimation of the ECSA by using the H_{upd} surface for Pt-skin surface formed by thermal annealing as reported recently,³⁷ for which CO stripping was found to be more accurate. Nevertheless, the D-Pt_xNi_{1-x} catalysts studied here underwent a dealloying process after thermal annealing, for which the H_{upd} method was found to be valid as well as the CO stripping method.³⁷

Measurements of ORR catalysis show that all the D-Pt_xNi_{1-x} exhibits significant enhancement of ORR activities over a state-

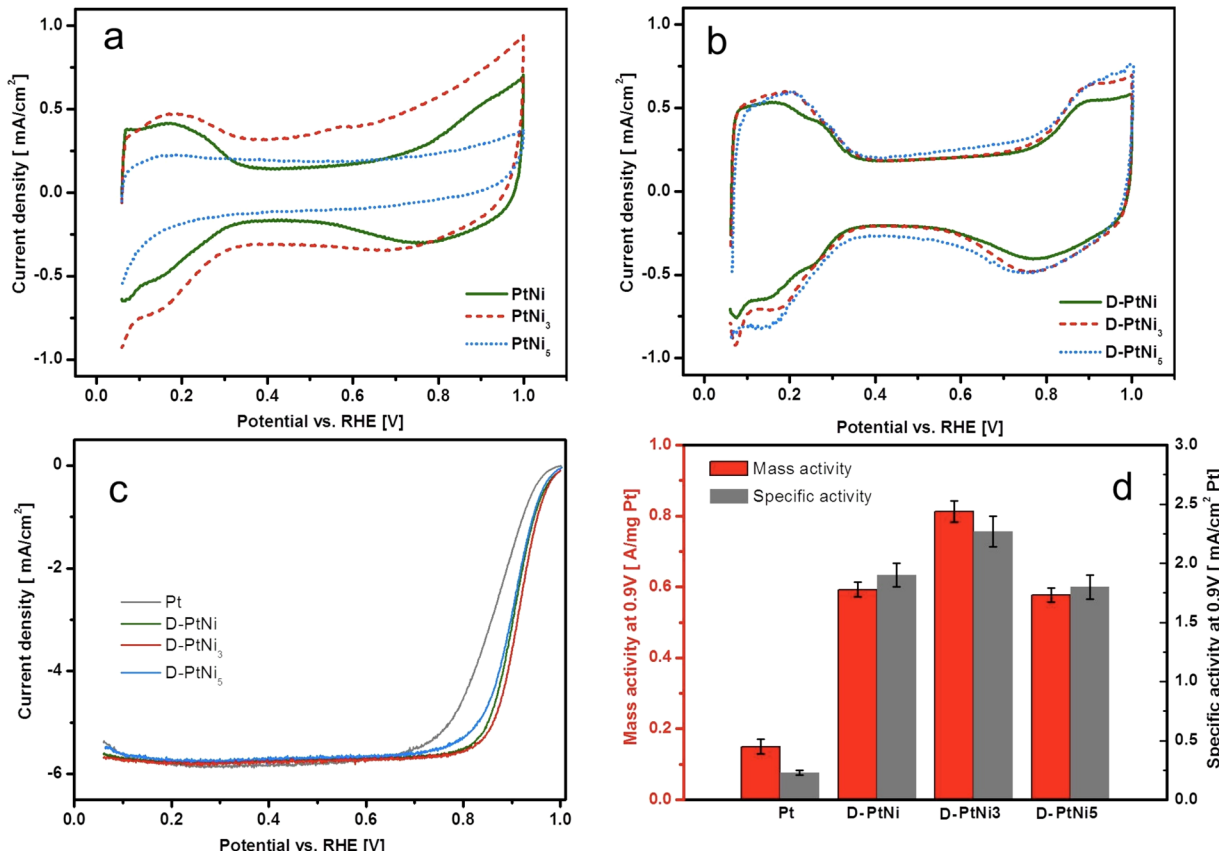


Figure 3. Electrochemical measurement of annealed carbon supported $\text{Pt}_x\text{Ni}_{1-x}$ catalysts on RDE electrodes (Pt loadings were around $12 \mu\text{g}/\text{cm}^2$): (a) Initial CV curves in N_2 -saturated 0.1 M HClO_4 aqueous solution, (b) CV curves in N_2 -saturated 0.1 M HClO_4 aqueous solution after electrochemical dealloying, (c) polarization curves of ORR by linear scanning voltammetry from 0.06 to 1.0 V at 5 mV/s in O_2 -saturated 0.1 M HClO_4 aqueous solution, (d) comparison of mass activities and specific activities at 0.9 V.

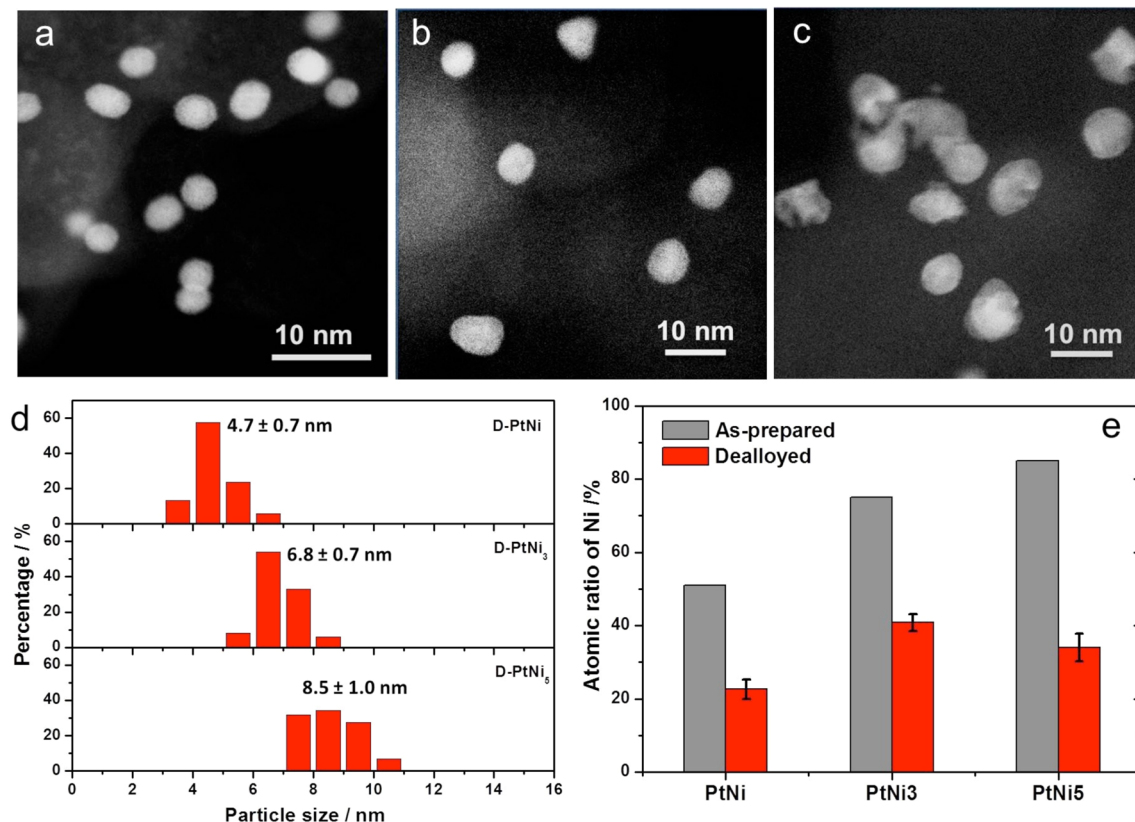


Figure 4. Morphology, size, and composition of D-Pt_xNi_{1-x} nanoparticles. (a–c) HAADF images of D-PtNi, D-PtNi₃, and D-PtNi₅ catalyst nanoparticles, respectively. (d) Particle size distribution analysis. (e) Compositional changes before and after electrochemical dealloying measured by EDX of a large collection of nanoparticles.

of-the-art commercial carbon supported Pt catalyst (~3 nm, Johnson Matthey), as indicated by positive shift of half-wave potentials in the polarization curves (Figure 3c). At 0.9 V, the D-Pt_xNi_{1-x} catalysts showed 4–5 fold enhancements in the mass activity compared with the benchmark Pt catalyst (Figure 3d). The highest mass activity (0.81 A/mg Pt) was achieved on the D-PtNi₃ catalyst, which is above 5 times of that of Pt catalyst (0.15 A/mg Pt). The specific activities of the catalysts also showed the highest value at D-PtNi₃/C catalyst (2.27 mA/cm² Pt), which is nearly 10 times of that of the Pt/C catalyst (0.23 mA/cm² Pt). Our result that the D-PtNi₃ nanoparticles shows the highest activity is somehow in good agreement with previous works on Pt_xNi_{1-x} nanoparticles³² as well as Pt_xNi_{1-x} thin film catalysts,^{23–25} where the best ORR activity was found at an initial Ni composition of around 70%.

To understand the origin of the composition-dependent activities shown in Figure 3d, we further investigated the structures of the dealloyed Pt_xNi_{1-x} catalysts at their catalytically active state. Figure 4a–c shows the HAADF images of the dealloyed Pt_xNi_{1-x} nanoparticles. The D-Pt_xNi_{1-x} nanoparticles generally show a spherical shape, except that some of D-PtNi₅ nanoparticles become somewhat irregular, showing increased surface roughness. This can be also seen from more bright-field TEM images (Figure S3 of the Supporting Information). All of the dealloyed catalysts show decreased particle sizes (Figure 4d) due to the loss of Ni atoms. A higher initial composition resulted in a larger extent of Ni dissolution and hence more significant size reduction. Therefore, the size difference among the three catalysts is greatly reduced.

EDX analysis showed that the average compositions of the D-PtNi, D-PtNi₃, and D-PtNi₅ catalysts changed to be Pt₇₇Ni₂₃, Pt₅₉Ni₄₁ and Pt₆₆Ni₃₄, respectively, suggesting no linear relationship between the initial composition and the composition after dealloy (Figure 4e). The higher the initial Ni composition, the larger the extent of Ni dissolution. The highest residual content of Ni in the D-PtNi₃ catalyst coincides well with its highest activity, which is consistent with a previous report.²⁷

It should be noted that the catalytic activities of the Pt alloy catalysts were more dependent on the near-surface compositions rather than the bulk compositions.¹³ Therefore, we further studied structural changes of individual nanoparticles by using aberration-corrected STEM measurement combined with EELS line analysis. After electrochemical dealloying, all of the dealloyed Pt–Ni nanoparticles revealed Pt-rich shells surrounding Pt–Ni alloy cores, as shown in Figure 5. Our EELS data evidence a distinct and, as we will show, a very important difference in the Ni distribution across the alloy cores. Figure 5a–d shows a typical high-resolution HAADF-STEM image and EELS line scan results across several nanoparticles of the D-PtNi catalyst. As expected from a simple core shell structure for a dealloyed bimetallic nanoparticle, the Ni composition shows a monotonic decrease from the particle center to the particle surface. Contrary to that, the D-PtNi₃ catalyst (Figure 5e–h) revealed an unusual Ni composition profile across the core, showing a previously undiscovered spherical enrichment of Ni at the near surface. Figure 5f,g present two perpendicular EELS line scan profiles across the nanoparticle shown in Figure 5e. Two off-center maxima of Ni intensity are clearly

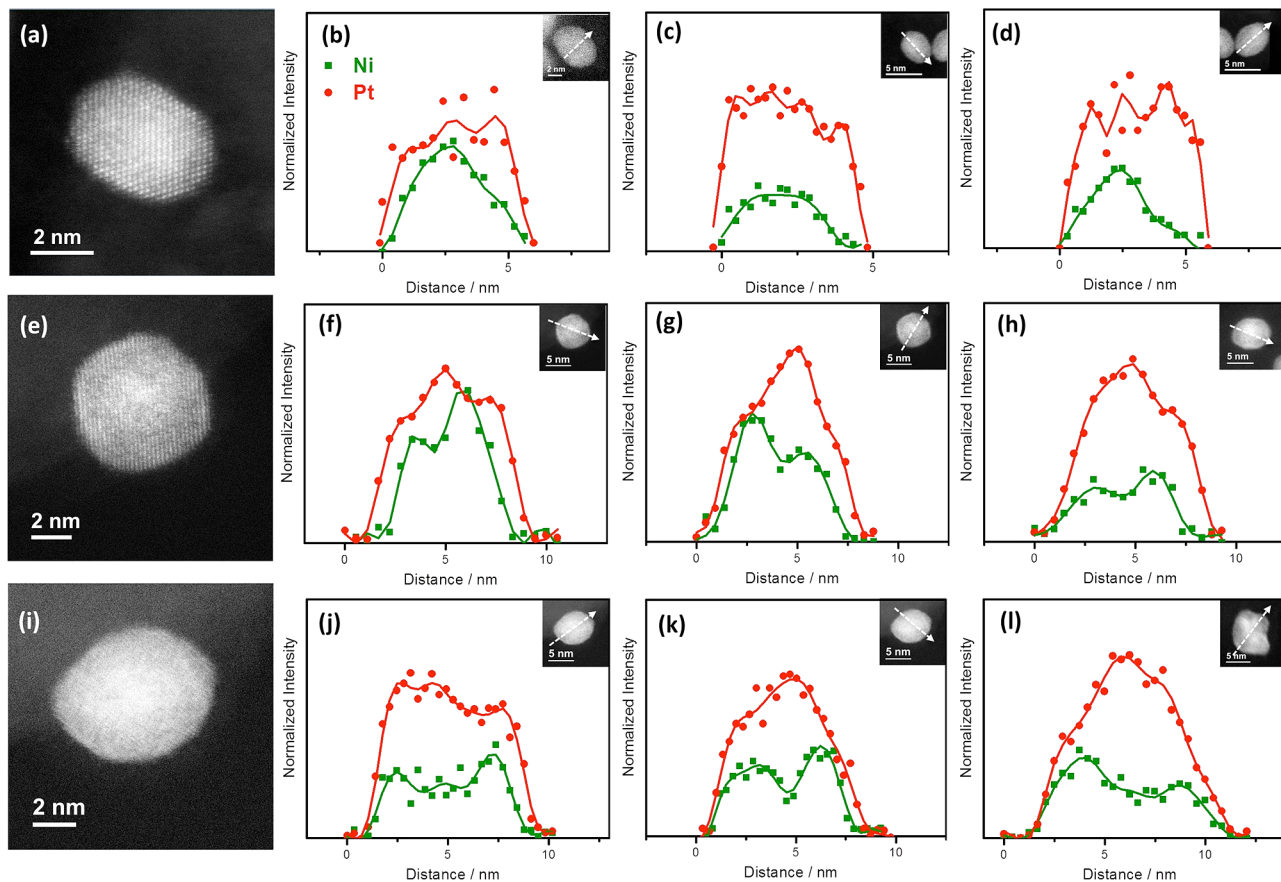


Figure 5. High-resolution HAADF-STEM images and EELS compositional line profiles of individual D-PtNi (a–d), D-PtNi₃ (e–h), and D-PtNi₅ (i–l) nanoparticles. The directions of the line profiles were plotted as dashed arrows in the corresponding nanoparticles. The EELS profiles are normalized with the elemental scattering factors, and hence the intensity ratios represent thickness-projected compositions.

Table 1. Summary of Key Near-Surface Structural Characteristics of the Dealloyed Pt_xNi_{1-x} Nanoparticles Derived from EELS Compositional Profiles

catalyst	Pt shell thickness ^a (nm)	maximum Ni composition ^b at the subsurface	depth of the Ni-composition maxima (nm)	mass activity (A/mg Pt)	specific activity (mA/cm ² Pt)	ECSA (m ² /g)
D-PtNi	0.5 ± 0.2	34 ± 7%	2.5 ± 0.4	0.59 ± 0.02	1.90 ± 0.10	29 ± 2
D-PtNi ₃	0.8 ± 0.2	47 ± 11%	2.6 ± 0.4	0.81 ± 0.03	2.27 ± 0.13	35 ± 3
D-PtNi ₅	0.4 ± 0.2	40 ± 11%	2.0 ± 0.3	0.58 ± 0.02	1.81 ± 0.10	33 ± 3

^aMeasured by the radius of Pt area minus the radius of Ni area above an intensity threshold of 10% of the maximum (for more details see Figure S5).

^bThe average Ni composition across the particle along electron beam direction.

discernible in both directions, which coincide with the inflection points in the Pt intensity profiles. In other words, a Ni-enriched inner shell is formed near the surface and sandwiched between a Ni-poorer core and a Pt outer shell. This Ni-enriched inner shell is found to be universal in the D-PtNi₃ catalyst (Figure 5h). In D-PtNi₅ catalyst (Figure 5i–l), it is interesting to note that the Ni-enriched inner shell is located closer to the surface compared with D-PtNi₃. Figure 5j–k again show two perpendicular EELS line scans from the nanoparticle shown in Figure 5i, which display the Ni compositional maxima located closer to the surface compared with D-PtNi₃ catalyst. More EELS line scan results of the dealloyed Pt_xNi_{1-x} nanoparticles are shown in Figure S4, and similar trends are revealed.

Table 1 compares the key near surface structural characteristics of the three catalysts derived from the EELS line profiles, including the Pt shell thickness, the composition, and depth of the Ni-enriched inner shell (for detailed method, see Figure S5

of the Supporting Information). The Pt shell thickness increases from 0.5 ± 0.2 nm (corresponding to ca. 2–3 monolayers) in D-PtNi catalyst to 0.8 ± 0.2 nm (ca. 3–5 monolayers) in D-PtNi₃, which is consistent with the previous report.²⁷ Further increases in the initial Ni composition, however, surprisingly lead to a decreased Pt shell thickness of 0.4 ± 0.2 nm (ca. 1–3 monolayers) in D-PtNi₅. This unexpected result underlines the complex relationship between initial composition and final geometrical structure in the dealloyed bimetallic nanoparticles. We suspect that the different Pt shell thicknesses could be explained in terms of the interplay between the extent of dissolution of Ni and the absolute numbers of residual Pt atoms. Increasing the initial Ni composition would result in a higher percolation of Ni atoms, and hence the Ni dissolution would penetrate deeper into the particle, leading to an increased Pt shell thickness. Further increases in the initial Ni content, however, would lead

to reduced absolute numbers of residual Pt atoms to form the shell and hence decreased Pt shell thickness.

Our most intriguing finding is that there is a strong tendency of near-surface spherical enrichment of Ni in the D-PtNi₃ and D-PtNi₅ catalyst, leading to the formation of Ni-enriched inner shells. While the D-PtNi catalyst shows a simple core–shell structure with a maximum Ni composition of 34 ± 7% at the particle center, the D-PtNi₃ catalyst shows a higher maximum Ni composition of 47 ± 11% at the formed Ni-enriched inner shell. At a higher initial Ni composition (in D-PtNi₅), the distance (d) between the Ni-enriched inner shell and the surface decreases, while the maximum Ni composition of the Ni-enriched inner shell decreases to 40 ± 11%. It should be noted that these values correspond to the average Ni ratios across the particle along electron beam direction. Due to the contribution of Pt shell above and below the Ni-enriched inner shell, there is an under-estimation of the true radial Ni compositions at the Ni-enriched inner shell. The larger the Pt shell thickness, the larger the under-estimation. As a result of this and our finding on the different Pt shell thickness, the trend in the maximum Ni composition shown in Table 1 remains valid. To gain understanding, Figure 6 shows the structural models reflecting the unusual core–shell fine structures of the dealloyed Pt_xNi_{1-x} nanoparticles.

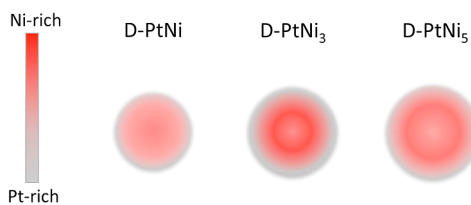


Figure 6. Structural model of distinctly different compositional core–shell fine structures of dealloyed Pt_xNi_{1-x} catalysts.

Previously, dealloyed Pt bimetallic nanoparticles were generally considered to form a simple core–shell structure with the core remaining unchanged before and after dealloying.^{21,27} Our result clearly demonstrates that there is rearrangement of the elemental distribution across the particle core during the dealloying of Pt_xNi_{1-x} nanoparticles, leading to Ni-enriched inner shells. The Ni-enriched inner shell is different from the surface-segregated “Pt-skin” structure in annealed Pt₃Ni surface reported by Stamenkovic et al.,^{13–15} where Pt is segregated to the topmost layer yet Ni is segregated exactly into the second layer due to the lower surface energy of Pt. In contrast, the Ni-enriched inner shell shown here is self-organized during dealloying of Pt alloys with a higher initial content of transition metals (such as PtNi₃ and PtNi₅ here), where near-surface enriched Ni is located at a depth up to several atomic layers.

The question then arises as to how the Ni-enriched inner shells formed during dealloying. A conventional view of the electrochemical dealloying suggested by Erlebacher et al.^{16,38,39} is described as two processes: (i) an initial rapid dissolution of the less noble alloy component from the outmost atomic layers, leading to a rough surface with vacancies, and (ii) a surface-diffusion of a residual more noble component, which causes the annihilation of vacancies. The competition of these two processes plays an important role in determining the morphology of dealloyed materials. In bulk bimetallic alloys, the diffusion of residual more noble atoms along the extended

surface is relatively slow, which results in Rayleigh surface instabilities promoting the formation of nanoporosity. In contrast, in small enough alloy nanoparticles, the lower average coordination of the noble metal atoms on the surface increases their surface diffusion rate, suppressing the formation of porosity and leading to solid core–shell nanoparticles. Indeed, it is reported that a minimum particle size is required to form porosity in the dealloyed nanoparticles (e.g., ~15 nm for PtNi₃⁴⁰ and ~30 nm for PtCu₃/PtCo₃⁴¹). This explains the formation of the generally nonporous dealloyed Pt_xNi_{1-x} nanoparticles shown here.

From the above view of the dealloying process, a monotonic drop in the composition of the less-noble component below the surface would be expected, which, however, is in conflict with the Ni-enriched inner shells observed here. We therefore suspect that additional processes need to be taken into account. First, during the electrochemical dealloying, oxygenated adsorbent on the particle surface would form by adsorption of water on Pt at the potential above ~0.6 V. This oxygenated adsorbent favors a surface segregation of Ni due to its strong chemisorption on Ni,⁴² leading to an adsorption-induced outward diffusion of Ni. However, the Pt shell formed by surface diffusion of residual Pt atoms would act as a barrier for the outward diffusion of Ni. The competition between these two processes may therefore result in an accumulation of Ni below the Pt shell, forming a Ni-enriched inner shell. A higher initial Ni composition could lead to a higher concentration of subsurface vacancies at the initial stage of dealloying, which enables an increased outward diffusion rate of Ni and thus in turn promotes a higher extent of Ni dissolution. Consequently, the formed Ni-enriched inner shell is closer to the surface but shows a lower Ni composition. Second, the annihilation of the vacancies formed in dealloying may induce an inward uphill diffusion of the residual undissolved Ni atoms at the near surface (inverse Kirkendall effect).^{43,44} Either of the above effects may contribute to the formation of the Ni-enriched inner shells. Further studies are needed to clarify the detailed mechanism.

The distinct core–shell fine structures shown here allow previously unachieved understanding on how the initial alloy compositions influence the ORR activities of Pt bimetallic catalysts. Basically, for the dealloyed Pt-bimetallic catalysts, there are mainly three factors that influence the specific activities: the Pt shell thickness,^{27,33} the surface roughness of Pt shell (i.e., the average coordinated number of surface Pt atoms),³³ and the composition of Ni beyond the Pt shell. A previous report suggested that a larger Pt shell thickness would result in a lower catalytic activity.²⁷ However, the present trend in Pt shell thickness cannot explain the highest catalytic activity of the D-PtNi₃ catalyst with the largest Pt shell thickness. The surface roughness of the Pt shell is related to the vacancies formed by dissolution of Ni, leading to a lower average coordination of Pt surface atoms, a stronger adsorption of intermediate oxygenated species, and hence a lower activity.^{5,33} It is expected that the surface roughness of the Pt shells would increase as the initial Ni composition increases due to more vacancies formed by dealloying, which might be evidenced by the appearance of apparently rough surfaces of some D-PtNi₅ nanoparticles (Figure 4c). The increase of surface roughness would result in a decrease of the specific activity, which may explain the lower activity of D-PtNi₅ compared to D-PtNi₃ but fails to account for the higher activity of D-PtNi₃ compared to D-PtNi. Our data strongly suggest that the compositional Ni

distribution below the Pt shell (up to \sim 10 atomic layers) plays a much more important role in the catalytic activities than previously assumed. Compared with the D-PtNi catalyst, the D-PtNi₃ catalyst exhibits a higher content of Ni at a comparable depth due to the presence of the Ni-enriched inner shell, leading to a higher extent of compressive strain over the Pt surface and hence a higher activity. For the D-PtNi₅ catalyst, the Ni-enriched inner shell comes closer to the surface and hence could potentially induce a further higher lattice strain in the Pt surface; however, the lower Ni composition at its Ni-enriched inner shell compared to D-PtNi₃ offsets the effect of the thinner Pt shell and thus results in a lower extent of the lattice strain. This effect, combined with its increased surface roughness, finally resulted in the lower activity of the D-PtNi₅ catalyst.

In summary, using aberration-corrected STEM combined with EELS line analysis, we uncovered unexpected and significantly different self-organized core–shell fine structures in the dealloyed Pt_xNi_{1-x} nanoparticles in terms of not only Pt shell thickness but also the Ni compositional distribution beneath the Pt shells. Attractively, a spherical Ni enrichment below the Pt shells was discovered, leading to the formation of Ni-enriched inner shells at a depth of 2–3 nm. The location and the composition of the Ni-enriched inner shells are strongly dependent on the initial alloy compositions. At a higher initial Ni composition, the Ni-enriched inner shell comes closer to the surface, while the Ni composition in the inner shell decreases. The disclosed Ni-enriched inner shell appears to play a critical role in determining the catalytic activities of the dealloyed Pt_xNi_{1-x} catalysts. The Ni-enriched inner shell would result in a higher extent of compressive strain on the Pt surface, leading to a maximum ORR activity on the D-PtNi₃ catalyst. This phenomenon is likely to be universal in dealloying of bimetallic alloys⁴⁵ and can be further applied to optimize Pt alloy catalysts with a broad range of compositions.

■ ASSOCIATED CONTENT

Supporting Information

Experimental details. Table S1: Compositions of carbon supported Pt_xNi_{1-x} catalysts measured by ICP-AES and EDX; Figure S1: particle size distributions and EDX spectra of as-prepared PtNi, PtNi₃, and PtNi₅ nanoparticles; Figure S2: Relationship between the lattice parameters and the compositions of annealed Pt_xNi_{1-x} catalysts; Figure S3: Bright-field TEM images of the dealloyed Pt_xNi_{1-x} catalyst; Figure S4: More EELS line scan results of dealloyed Pt_xNi_{1-x} nanoparticles: (a) D-PtNi (b) D-PtNi₃ (c) D-PtNi₅; Figure S5: Methods for EELS line profiles measurement, evaluation of Pt shell thickness, composition, and depth of near surface enriched Ni inner-shell in dealloyed Pt_xNi_{1-x} catalyst. This material is available free of charge via the Internet at <http://pubs.acs.org>.

■ AUTHOR INFORMATION

Corresponding Author

*E-mail: pstrasser@tu-berlin.de.

Notes

The authors declare no competing financial interest.

■ ACKNOWLEDGMENTS

We thank Dr. Frederick T. Wagner for valuable discussions. We thank the Zentraleinrichtung für Elektronenmikroskopie (Zelmi) of the Technical University Berlin for their support

with TEM and EDX techniques. This work was supported by U.S. DOE EERE award DE-EE0000458 via subcontract through General Motors and by Ernst Ruska Center for Microscopy and Spectroscopy with Electrons, Forschungszentrum Juelich GmbH, Germany. P.S. acknowledges financial support through the Cluster of Excellence in Catalysis (UniCat) funded by DFG and managed by TU Berlin.

■ REFERENCES

- (1) Gasteiger, H. A.; Markovic, N. M. *Science* **2009**, 324, 48.
- (2) Wagner, F. T.; Lakshmanan, B.; Mathias, M. F. *J. Phys. Chem. Lett.* **2010**, 1, 2204.
- (3) Gasteiger, H. A.; Kocha, S. S.; Sompalli, B.; Wagner, F. T. *Appl. Catal., B* **2005**, 56, 9.
- (4) Lee, S. W.; Chen, S.; Suntivich, J.; Sasaki, K.; Adzic, R. R.; Shao-Horn, Y. *J. Phys. Chem. Lett.* **2010**, 1, 1316.
- (5) Cai, Y.; Ma, C.; Zhu, Y. M.; Wang, J. X.; Adzic, R. R. *Langmuir* **2011**, 27, 8540.
- (6) Stamenkovic, V.; Mun, B. S.; Mayrhofer, K. J. J.; Ross, P. N.; Markovic, N. M.; Rossmeisl, J.; Greeley, J.; Norskov, J. K. *Angew. Chem., Int. Ed.* **2006**, 45, 2897.
- (7) Greeley, J.; Mavrikakis, M. *Nat. Mater.* **2004**, 3, 810.
- (8) Zhang, J.; Mo, Y.; Vukmirovic, M. B.; Klie, R.; Sasaki, K.; Adzic, R. R. *J. Phys. Chem. B* **2004**, 108, 10955.
- (9) Zhang, J. L.; Vukmirovic, M. B.; Sasaki, K.; Nilekar, A. U.; Mavrikakis, M.; Adzic, R. R. *J. Am. Chem. Soc.* **2005**, 127, 12480.
- (10) Zhang, J. L.; Vukmirovic, M. B.; Xu, Y.; Mavrikakis, M.; Adzic, R. R. *Angew. Chem., Int. Ed.* **2005**, 44, 2132.
- (11) Adzic, R. R.; Zhang, J.; Sasaki, K.; Vukmirovic, M. B.; Shao, M.; Wang, J. X.; Nilekar, A. U.; Mavrikakis, M.; Valerio, J. A.; Uribe, F. *Top. Catal.* **2007**, 46, 249.
- (12) Ghosh, T.; Vukmirovic, M. B.; DiSalvo, F. J.; Adzic, R. R. *J. Am. Chem. Soc.* **2010**, 132, 906.
- (13) Stamenkovic, V. R.; Mun, B. S.; Mayrhofer, K. J. J.; Ross, P. N.; Markovic, N. M. *J. Am. Chem. Soc.* **2006**, 128, 8813.
- (14) Stamenkovic, V. R.; Fowler, B.; Mun, B. S.; Wang, G. F.; Ross, P. N.; Lucas, C. A.; Markovic, N. M. *Science* **2007**, 315, 493.
- (15) Stamenkovic, V. R.; Mun, B. S.; Arenz, M.; Mayrhofer, K. J. J.; Lucas, C. A.; Wang, G. F.; Ross, P. N.; Markovic, N. M. *Nat. Mater.* **2007**, 6, 241.
- (16) Erlebacher, J.; Aziz, M. J.; Karma, A.; Dimitrov, N.; Sieradzki, K. *Nature* **2001**, 410, 450.
- (17) Ding, Y.; Chen, M. W.; Erlebacher, J. *J. Am. Chem. Soc.* **2004**, 126, 6876.
- (18) Snyder, J.; Fujita, T.; Chen, M. W.; Erlebacher, J. *Nat. Mater.* **2010**, 9, 904.
- (19) Koh, S.; Strasser, P. *J. Am. Chem. Soc.* **2007**, 129, 12624.
- (20) Srivastava, R.; Mani, P.; Hahn, N.; Strasser, P. *Angew. Chem., Int. Ed.* **2007**, 46, 8988.
- (21) Strasser, P.; Koh, S.; Anniyev, T.; Greeley, J.; More, K.; Yu, C. F.; Liu, Z. C.; Kaya, S.; Nordlund, D.; Ogasawara, H.; Toney, M. F.; Nilsson, A. *Nat. Chem.* **2010**, 2, 454.
- (22) Bonakdarpour, A.; Lobel, R.; Atanasoski, R. T.; Vernstrom, G. D.; Schmoeckel, A. K.; Debe, M. K.; Dahn, J. R. *J. Electrochem. Soc.* **2006**, 153, A1835.
- (23) Debe, M. K.; Steinbach, A. J.; Vernstrom, G. D.; Hendricks, S. M.; Kurkowski, M. J.; Atanasoski, R. T.; Kadera, P.; Stevens, D. A.; Sanderson, R. J.; Marvel, E.; Dahn, J. R. *J. Electrochem. Soc.* **2011**, 158, B910.
- (24) Liu, G. C. K.; Stevens, D. A.; Burns, J. C.; Sanderson, R. J.; Vernstrom, G. D.; Atanasoski, R. T.; Debe, M. K.; Dahn, J. R. *J. Electrochem. Soc.* **2011**, 158, B919.
- (25) Stevens, D. A.; Mehrotra, R.; Sanderson, R. J.; Vernstrom, G. D.; Atanasoski, R. T.; Debe, M. K.; Dahn, J. R. *J. Electrochem. Soc.* **2011**, 158, B905.
- (26) Stevens, D. A.; Wang, S.; Sanderson, R. J.; Liu, G. C. K.; Vernstrom, G. D.; Atanasoski, R. T.; Debe, M. K.; Dahn, J. R. *J. Electrochem. Soc.* **2011**, 158, B899.

- (27) Wang, C.; Chi, M. F.; Wang, G. F.; van der Vliet, D.; Li, D. G.; More, K.; Wang, H. H.; Schlueter, J. A.; Markovic, N. M.; Stamenkovic, V. R. *Adv. Funct. Mater.* **2011**, *21*, 147.
- (28) Oezaslan, M.; Hasche, F.; Strasser, P. *J. Electrochem. Soc.* **2012**, *159*, B444.
- (29) Oezaslan, M.; Hasche, F.; Strasser, P. *J. Electrochem. Soc.* **2012**, *159*, B394.
- (30) Koh, S.; Hahn, N.; Yu, C. F.; Strasser, P. *J. Electrochem. Soc.* **2008**, *155*, B1281.
- (31) Liu, Y.; Hangarter, C. M.; Bertocci, U.; Moffat, T. P. *J. Phys. Chem. C* **2012**, *116*, 7848.
- (32) Rudi, S.; Tuaev, X.; Strasser, P. *Electrocatalysis* **2012**, DOI: 10.1007/s12678-012-0098-x.
- (33) Wang, C.; Chi, M. F.; Li, D. G.; Strmcnik, D.; van der Vliett, D.; Wang, G. F.; Komanicky, V.; Chang, K. C.; Paulikas, A. P.; Tripkovic, D.; Pearson, J.; More, K. L.; Markovic, N. M.; Stamenkovic, V. R. *J. Am. Chem. Soc.* **2011**, *133*, 14396.
- (34) Ahrenstorff, K.; Albrecht, O.; Heller, H.; Kornowski, A.; Gorlitz, D.; Weller, H. *Small* **2007**, *3*, 271.
- (35) Ahrenstorff, K.; Heller, H.; Kornowski, A.; Broekaert, J. A. C.; Weller, H. *Adv. Funct. Mater.* **2008**, *18*, 3850.
- (36) Toda, T.; Igarashi, H.; Uchida, H.; Watanabe, M. *J. Electrochem. Soc.* **1999**, *146*, 3750.
- (37) van der Vliet, D. F.; Wang, C.; Li, D. G.; Paulikas, A. P.; Greeley, J.; Rankin, R. B.; Strmcnik, D.; Tripkovic, D.; Markovic, N. M.; Stamenkovic, V. R. *Angew. Chem., Int. Ed.* **2012**, *51*, 3139.
- (38) Erlebacher, J. *J. Electrochem. Soc.* **2004**, *151*, C614.
- (39) Erlebacher, J. *Phys. Rev. Lett.* **2011**, *106*, 225504.
- (40) Snyder, J.; McCue, I.; Livi, K.; Erlebacher, J. *J. Am. Chem. Soc.* **2012**, *134*, 8633.
- (41) Oezaslan, M.; Heggen, M.; Strasser, P. *J. Am. Chem. Soc.* **2012**, *134*, 514.
- (42) Mayrhofer, K. J. J.; Hartl, K.; Juhart, V.; Arenz, M. *J. Am. Chem. Soc.* **2009**, *131*, 16348.
- (43) Marwick, A. D. *J. Phys. F: Metal Phys.* **1978**, *8*, 1849.
- (44) Yu, H. C.; Yeon, D. H.; Li, X.; Thornton, K. *Acta Mater.* **2009**, *57*, 5348.
- (45) Heggen, M.; Oezaslan, M.; Strasser, P. *J. Phys. Chem. C* **2012**, *116*, 19073–19083.